

Vivim: a Video Vision Mamba for Medical Video Object Segmentation

Yijun Yang¹, Zhaohu Xing¹, Chunwang Huang³, and Lei Zhu^{1,2} (✉)

¹ The Hong Kong University of Science and Technology (Guangzhou)
yyang018@connect.hkust-gz.edu.cn

² The Hong Kong University of Science and Technology

³ Department of Ultrasound, Guangdong Provincial People’s Hospital, Southern Medical University

Abstract. Traditional convolutional neural networks have a limited receptive field while transformer-based networks are mediocre in constructing long-term dependency from the perspective of computational complexity. Such the bottleneck poses a significant challenge when processing long sequences in video analysis tasks. Very recently, the state space models (SSMs) with efficient hardware-aware designs, famous by Mamba, have exhibited impressive achievements in long sequence modeling, which facilitates the development of deep neural networks on many vision tasks. To better capture available dynamic cues in video frames, this paper presents a generic Video Vision Mamba-based framework, dubbed as **Vivim**, for medical video object segmentation tasks. Our Vivim can effectively compress the long-term spatiotemporal representation into sequences at varying scales by our designed Temporal Mamba Block. We also introduce a boundary-aware constraint to enhance the discriminative ability of Vivim on ambiguous lesions in medical images. Extensive experiments on thyroid segmentation in ultrasound videos and polyp segmentation in colonoscopy videos demonstrate the effectiveness and efficiency of our Vivim, superior to existing methods. The code is available at: <https://github.com/scott-yjyang/Vivim>.

Keywords: State space model · Mamba · Video object segmentation · Ultrasound videos.

1 Introduction

Automatic segmentation of lesions and tissues in medical videos is essential for computer-aided clinical examination and treatment [13], such as ultrasound lesion segmentation, polyp segmentation. However, segmenting medical objects is usually challenging due to inherent factors, including ambiguous lesion boundaries, inhomogeneous distributions, diverse motion patterns, and dynamic changes in tissue sizes over time [20]. To overcome such bottlenecks, expanding the deep model’s receptive field in the spatiotemporal space is highly desired for more object references. Traditional convolutional neural networks [33,12,11,30] often struggle to capture global information compared to recent transformer-based

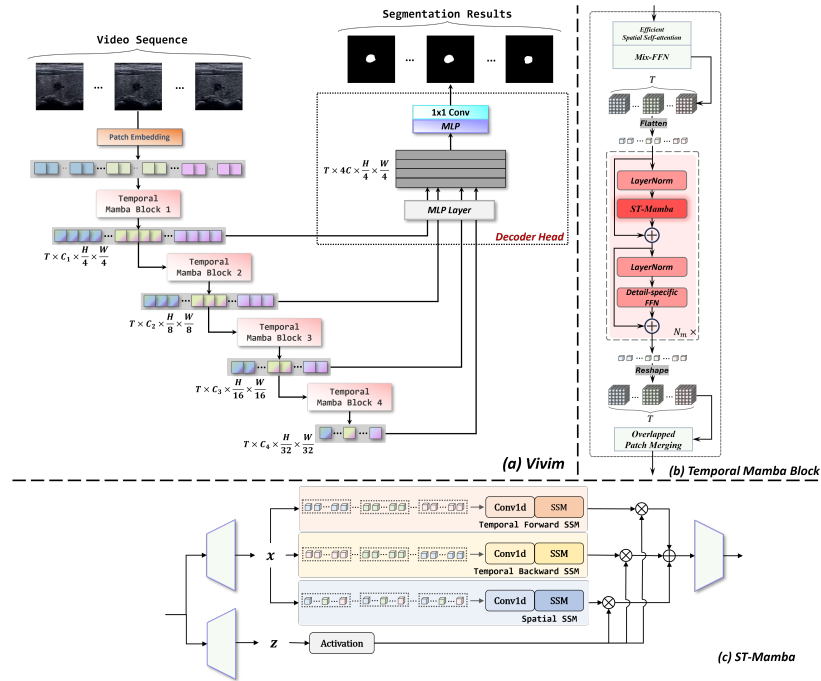


Fig. 1. (a) The overview of the proposed Vivim. (b) The fundamental building block of Vivim, namely Temporal Mamba Block. (c) ST-Mamba incorporates spatiotemporal sequence modeling for video vision tasks in a multi-way spirit.

architectures. The transformer architecture, which utilizes the Multi-Head Self Attention (MSA) [26] to extract global information, has attracted much attention from the community of video object segmentation [32,1,19]. Considering that neighboring frames offer beneficial hints to the segmentation, these methods usually introduce some elaborated modules on the self-attention mechanism to exploit the temporal information. However, its quadratic computation complexity impedes further application to clinical scenarios. The dramatically increasing number of tokens in long sequences from videos leads to significant computational burdens when adopting MSA for modeling temporal information [1].

Very recently, to address the ill-posed issue concerning long sequence modeling, Mamba [10], inspired by state space models (SSMs) [17], has been developed. Its main idea is to efficiently capture long-range dependencies by implementing a selective scan mechanism for 1-D sequence interaction. Based on this, U-Mamba [21] designed a hybrid CNN-SSM block, which is mainly composed of Mamba modules, to handle the long sequences in biomedical image segmentation tasks. Vision Mamba [34] provided a new generic vision backbone with bidirectional Mamba blocks on image classification and semantic segmentation tasks. As suggested by them, relying on the self-attention module is not necessary to

achieve efficient visual representation learning. Thus, it can be easily replaced by Mamba when exploring long-term temporal dependency in video scenarios.

Motivated by this, **1) we present an SSMS-based framework Vivim that integrates Mamba into the multi-level transformer architecture** to exploit spatiotemporal information in videos with linear complexity. *To the best of our knowledge, this is the first work to incorporate SSMS into the task of medical video object segmentation, facilitating faster and greater performance.* In our Vivim, drawing inspiration from the architecture of modern transformer blocks, **2) we design a novel Temporal Mamba Block.** A hierarchical encoder consisting of multiple Temporal Mamba Blocks is introduced to investigate the correlation between spatial and temporal dependency at various scales. As the structured state space sequence models with selective scan (S6) [10] causally process input data, they can only capture information within the scanned portion of the data. This aligns S6 with NLP and video tasks involving temporal data but poses challenges when addressing non-causal data like 2D images within medical videos. To this end, **3) the structured state space sequence model with spatiotemporal selective scan, ST-Mamba, is designed and incorporated into each scale of the model’s encoder,** replacing the self-attention or window-attention module to achieve efficient video visual representation learning. Finally, we employ a boundary-aware constraint to improve the discrimination of Vivim on ambiguous tissues in medical videos. In this work, **4) we collect a thyroid segmentation dataset VTUS with 100 annotated ultrasound videos** to facilitate the benchmarking evaluation. We conduct extensive experiments on VTUS and polyp colonoscopy videos. The superior results validate the effectiveness and universality of our framework Vivim.

2 Method

In this part, we elaborate on a Mamba-based solution Vivim for medical video object segmentation tasks. Our Vivim mainly consists of two modules: A hierarchical encoder with the stacked Temporal Mamba Blocks to extract coarse and fine feature sequences at different scales, and a lightweight CNN-based decoder head to fuse multi-level feature sequences and predict segmentation masks. Fig. 1 (a) displays the flowchart of our proposed Vivim.

Given a video clip with T frames, *i.e.*, $\mathbf{V} = \{I_1, \dots, I_T\}$, we first divide these frames into patches of size 4×4 by overlapped patch embedding. We then feed the sequence of patches into our hierarchical Temporal Mamba Encoder to obtain multi-level spatiotemporal features with resolution $\{1/4, 1/8, 1/16, 1/32\}$ of the original frame. Finally, we pass multi-level features to the CNN-based decoder head to predict the segmentation results. Please refer to the following sections for more details about our proposed module.

2.1 Overall architecture

Hierarchical feature representation. Multi-level features provide both high-resolution coarse features and low-resolution fine-grained features that significantly improve the segmentation results, especially for medical images. To this

end, unlike Vivit [1], our encoder extracts multi-level multi-scale features given input video frames. Specifically, we perform patch merging frame-by-frame at the end of each Temporal Mamba Block, resulting in the i -th feature embedding \mathcal{F}_i with a resolution of $\frac{H}{2^{i+1}} \times \frac{W}{2^{i+1}}$.

Temporal Mamba Block. Exploring temporal information is critically important for medical video object segmentation by providing dynamic appearance and motion cues. However, MSA in vanilla Transformer architectures has quadratic complexity concerning the number of tokens [26]. This complexity is pertinent for long feature sequences from videos, as the number of tokens increases linearly with the number of input frames. Motivated by this, we develop a more efficient block, Temporal Mamba Block, to simultaneously exploit spatial and temporal information by structured state space sequence models.

As illustrated in Fig. 1 (b), in the Temporal Mamba Block, an efficient spatial-only self-attention module is first introduced to provide the initial aggregation of spatial information followed by a Mix-FeedForward layer. We leverage the sequence reduction process introduced in [29,27] to improve its efficiency. For the i -level feature embedding $\mathcal{F}_i \in \mathbb{R}^{T \times C_i \times H \times W}$ of the given video clip, we transpose the channel and temporal dimension, and flatten the spatiotemporal feature embedding into 1D long sequence $h_i \in \mathbb{R}^{C_i \times THW}$. Then, the flattened sequence h_i is fed into layers of a Spatio-Temporal Mamba module (ST-Mamba) and a Detail-Specific Feedforward (DSF). The ST-Mamba module establishes the intra- and inter-frame long-range dependencies while the DSF preserves fine-grained details by a depth-wise convolution with a kernel size of $3 \times 3 \times 3$. The procedure in the stacked Mamba Layer can be defined as, where $l \in [1, N_m]$:

$$h^l = \text{ST-Mamba}(\text{LN}(h^{l-1})) + h^{l-1}, h^l = \text{DSF}(\text{LN}(h^l)) + h^l. \quad (1)$$

Finally, we return the output feature sequence to the original shape and employ overlapped patch merging to down-sampling the feature embedding.

Decoder. To predict the segmentation mask from the multi-level feature embeddings, we introduce a CNN-based segmentation head. While our hierarchical Temporal Mamba encoder has a large effective receptive field across spatial and temporal axes, the CNN-based segmentation head further refines the details of local regions. To be specific, the multi-level features $\{\mathcal{F}_1, \mathcal{F}_2, \mathcal{F}_3, \mathcal{F}_4\}$ from the temporal mamba blocks are passed into an MLP layer to unify the channel dimension. These unified features are up-sampled to the same resolution and concatenated together. Third, a MLP layer is adopted to fuse the concatenated features \mathcal{F} . Finally, The fused feature goes through a 1×1 convolutional layer to predict the segmentation mask \mathcal{M} . The segmentation loss \mathcal{L}_{seg} consisting of pixel-wise cross-entropy loss and IoU loss is applied during training.

2.2 Spatiotemporal Selective Scan

Despite the causal nature of S6 for temporal data, videos differ from texts in that they not only contain temporal redundant information but also accumulate non-causal 2D spatial information. To address this problem of adapting to

non-causal data, we introduce ST-Mamba, which incorporates spatiotemporal sequence modeling for video vision tasks, as shown in Fig. 1 (c).

Specifically, to explicitly explore the relationship among frames, we first unfold patches of each frame along rows and columns into sequences, and then concatenate the frame sequences to constitute the video sequence $h_i^t \in \mathbb{R}^{C_i \times T(HW)}$. We parallelly proceed with scanning along the forward and backward directions to explore bidirectional temporal dependency. This approach allows the models to compensate for each other’s receptive fields without significantly increasing computational complexity. Simultaneously, we stack patches along the temporal axis and construct the spatial sequence $h_i^s \in \mathbb{R}^{C_i \times (HW)^T}$. We proceed with scanning to integrate information of each pixel from all frames. The spatiotemporal selective scan explicitly considers both single-frame spatial coherence and cross-frame coherence, and leverages parallel SSMS to establish the intra- and inter-frame long-range dependencies. The structured state space sequence models with spatiotemporal selective scan (ST-Mamba), serve as the core element to construct the Temporal Mamba block, which constitutes the fundamental building block of Vivim.

Computational-Efficiency. SSMS in ST-Mamba and self-attention in Transformer both provide a crucial solution to model spatiotemporal context adaptively. Given a video visual sequence $\mathbf{K} \in \mathbb{R}^{1 \times T \times M \times D}$, the computation complexity of a global self-attention and SSM are:

$$\Omega(\text{self-attention}) = 4(\text{TM})\text{D}^2 + 2(\text{TM})^2\text{D}, \quad \Omega(\text{SSM}) = 4(\text{TM})(2\text{D})\text{N} + (\text{TM})(2\text{D})\text{N}^2, \quad (2)$$

where the default expansion ratio is 2, N is a fixed parameter and set to 16. As observed, self-attention is quadratic to the whole video sequence length (TM), and SSM is linear to that. Such computational efficiency makes ST-Mamba a better solution for long-term video applications.

2.3 Boundary-aware Constraint

The network optimized only by the segmentation supervision tends to generate ambiguous and unstructured predictions. To mitigate this problem, we introduce a boundary-aware constraint inspired by InverseForm [4] to enforce the predicted boundary structure. Specifically, we address this constraint task by optimizing the affine transformation between ground-truth edges and edges in feature maps towards identity transformation matrix. The ground truth edges within the patches are derived from applying the Sobel operator [5] on ground truth masks, while the feature patches are processed by an auxiliary boundary head. We calculate the affine transform matrix $\hat{\theta}_i$ for the i -th patch between ground-truth edges and processed feature patches with a pre-trained MLP. This MLP is trained in advance with edge masks and not optimized during our method’s training. We optimize this affine transform matrix towards identity matrix \mathbb{I} by:

$$\mathcal{L}_{affine} = \frac{1}{N_p} \sum_{i=1}^{N_p} \left| \hat{\theta}_i - \mathbb{I} \right|_F, \quad (3)$$

Table 1. Quantitative comparison with state-of-the-art methods on our VTUS dataset.

Methods	Venue	Type	Dice	Jaccard	Precision	Recall	FPS
UNet [24]	<i>MICCAI</i> ₁₅	image	0.6662	0.5328	0.6703	0.7471	88.18
UNet++ [33]	<i>DLMIA</i> ₁₈	image	0.7656	0.6486	0.7441	0.8496	40.90
TransUNet [6]	<i>arXiv</i> ₂₁	image	0.7461	0.6250	0.7468	0.8321	65.10
SETR [32]	<i>CVPR</i> ₂₁	image	0.7288	0.6010	0.7399	0.8089	21.61
DAF [28]	<i>MICCAI</i> ₁₈	image	0.7716	0.6583	0.7046	0.8599	47.62
OSVOS [23]	<i>CVPR</i> ₁₇	video	0.7769	0.6754	0.7895	0.8241	27.25
ViViT [1]	<i>ICCV</i> ₂₁	video	0.7610	0.6459	0.7789	0.8252	24.33
STM [22]	<i>ICCV</i> ₁₉	video	0.7898	0.6897	0.8112	0.8251	23.17
AFB-URR [19]	<i>NIPS</i> ₂₀	video	0.7930	0.6957	0.7764	0.8429	11.84
DPSTT [18]	<i>MICCAI</i> ₂₂	video	0.8063	0.7117	0.8238	0.8352	30.50
Our method	--	video	0.8304	0.7372	0.8321	0.8706	35.33

where N_p denotes the number of patches and $|\cdot|_F$ is Frobenius norm.

We also calculate the binary cross entropy loss \mathcal{L}_{bce} between the whole predicted boundary and corresponding ground truths to further optimize the boundary detection. Finally, the overall loss to optimize during training is as follows, where the scaling parameters λ_1, λ_2 are both empirically set as 0.3:

$$\mathcal{L} = \mathcal{L}_{seg} + \lambda_1 \mathcal{L}_{affine} + \lambda_2 \mathcal{L}_{bce}. \quad (4)$$

3 Experiments

3.1 Dataset and Implementation

We evaluate our Vivim on two medical video object segmentation tasks, *i.e.*, video thyroid ultrasound segmentation and video polyp segmentation.

Video thyroid segmentation. We collect a video thyroid ultrasound segmentation dataset *VTUS*. *VTUS* comprises 100 video sequences, one video sequence per patient, 9342 frames annotated with pixel-level ground truth by three experts. The entire dataset is partitioned into training and test sets by 7:3, yielding a total of 70 training videos, 30 test videos. The detailed statistics are described in the *Supplementary Material*.

Video polyp segmentation. We adopt four widely used polyp datasets, including image-based Kvasir [14] and video-based CVC-300 [3], CVC-612 [2] and ASU-Mayo [25]. Following the same protocol as [16], we train our model on Kvasir, ASU-Mayo and the training sets of CVC-300 and CVC-612, and conduct three experiments on test datasets CVC-300-TV, CVC-612-V and CVC-612-T.

Implementation details. The proposed framework was trained on one NVIDIA RTX 3090 GPU and implemented on the Pytorch platform. Our framework is empirically trained for 100 epochs in an end-to-end way and the Adam optimizer is applied. The initial learning rate is set to 1×10^{-4} and decayed to 1×10^{-6} . During training, we resize the video frames to 256×256 , and feed a batch of 4 video clips, each of which has 5 frames, into the network for each iteration.

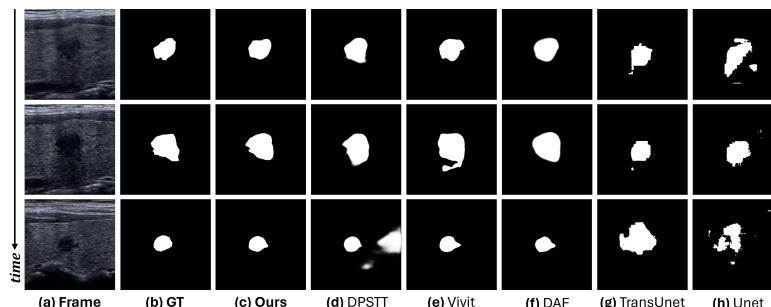


Fig. 2. Visual comparison on VTUS with image- and video-based methods.

Table 2. Quantitative results on three video polyp datasets. The best scores are highlighted in **bold**. \uparrow indicates the higher the score the better, and vice versa.

Metrics	2018~2019			2020~2021			2024
	UNet MICCAI [24]	UNet++ TMI [33]	ResUNet ISM [15]	ACSNet MICCAI [31]	PraNet MICCAI [9]	PNS-Net MICCAI [16]	Vivim (Ours)
CVC-300-TV							
maxDice \uparrow	0.639	0.649	0.535	0.738	0.739	0.840	0.901
maxSpe \uparrow	0.963	0.944	0.852	0.987	0.993	0.996	0.997
maxIoU \uparrow	0.525	0.539	0.412	0.632	0.645	0.745	0.831
$S_o \uparrow$	0.793	0.796	0.703	0.837	0.833	0.909	0.928
$E_\phi \uparrow$	0.826	0.831	0.718	0.871	0.852	0.921	0.958
$MAE \downarrow$	0.027	0.024	0.052	0.016	0.016	0.013	0.008
CVC-612-V							
maxDice \uparrow	0.725	0.684	0.752	0.804	0.869	0.873	0.897
maxSpe \uparrow	0.971	0.952	0.939	0.929	0.983	0.991	0.996
maxIoU \uparrow	0.610	0.570	0.648	0.712	0.799	0.800	0.829
$S_o \uparrow$	0.826	0.805	0.829	0.847	0.915	0.923	0.940
$E_\phi \uparrow$	0.855	0.830	0.877	0.887	0.936	0.944	0.971
$MAE \downarrow$	0.023	0.025	0.023	0.054	0.013	0.012	0.010
CVC-612-T							
maxDice \uparrow	0.729	0.740	0.617	0.782	0.852	0.860	0.872
maxSpe \uparrow	0.971	0.975	0.950	0.975	0.986	0.992	0.995
maxIoU \uparrow	0.635	0.635	0.514	0.700	0.786	0.795	0.810
$S_o \uparrow$	0.810	0.800	0.727	0.838	0.886	0.903	0.915
$E_\phi \uparrow$	0.836	0.817	0.758	0.864	0.904	0.903	0.921
$MAE \downarrow$	0.058	0.059	0.084	0.053	0.038	0.038	0.033

3.2 Comparison with state-of-the-art methods

Video thyroid US segmentation. We employed four segmentation evaluation metrics, including Dice, Jaccard, Precision and Recall; for their precise definitions, please refer to [28]. We also report the inference speed performance by computing the number of frames per second (FPS).

As shown in Tab. 1, we quantitatively compare our method with many state-of-the-art methods on VTUS dataset. These methods including popular medical image segmentation methods (UNet [24], UNet++ [33], TransUNet [6], SETR [32], DAF [28]), and video object segmentation methods (OSVOS [23], ViViT [1], STM [22], AFB-URR [19], DPSTT [18]). For the fairness of comparisons, we reproduce these methods following their publicly available codes. We can observe that video-based methods tend to outperform image-based methods as evidenced by their better performance. This suggests that the exploration of temporal information offers significant advantages for segmenting thyroid nodules in ultrasound videos. More importantly, among all image-based and video-based segmentation methods, our Vivim has achieved the highest performance across all scores by a considerable margin. Our Vivim also has the best run-time among all video-based methods observed from FPS. As displayed in Fig. 2, we visualize the thyroid segmentation results on the selected frames. Our model can better locate and segment the target lesions with more accurate boundaries.

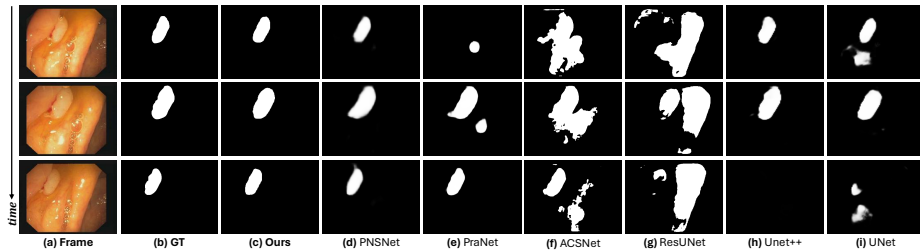


Fig. 3. Qualitative results on the selected frames of CVC-612-T. Our Vivim can better locate and segment polyps with more accurate boundaries.

Table 3. Ablation study on our Vivim design.

	ST-Mamba			Boundary Constraint	VTUS			
	T^f	T^b	S		Dice \uparrow	Jaccard \uparrow	Precision \uparrow	Recall \uparrow
basic	-	-	-	-	0.8144	0.7188	0.8040	0.8572
C1	✓	-	-	-	0.8159	0.7216	0.8170	0.8704
C2	✓	✓	-	-	0.8213	0.7264	0.8239	0.8670
C3	✓	✓	✓	-	0.8259	0.7310	0.8255	0.8753
Ours	✓	✓	✓	✓	0.8304	0.7372	0.8321	0.8706

Video polyp segmentation. We adopt six metrics following [16], *i.e.*, maximum Dice (maxDice), maximum specificity (maxSpe), maximum IoU (maxIoU), S-measure [7] (S_α), E-measure [8] (E_ϕ), and mean absolute error (MAE).

we compare our method with existing methods as summarized in Tab. 2, including UNet [24], UNet++ [33], ResUNet [15], ACSNet [31], PraNet [9] and PNS-Net [16]. We conduct three experiments on CVC-300-TV, CVC-612-V and CVC-612-T to validate the model’s performance. On CVC-300-TV, our Vivim achieves remarkable performance and outperforms all methods by a large margin (*e.g.*, 6.1% in maxDice, 8.6% in maxIoU). On CVC-612-V and CVC-612-T, our Vivim consistently outperforms other SOTAs, especially 2.4% and 1.2% in maxDice, respectively. We also visualize the polyp segmentation results on the consecutive frames of CVC-612-T in Fig. 3.

3.3 Ablation Study

Extensive experiments are conducted on VTUS dataset to evaluate the effectiveness of our major components. To do so, we construct four baseline networks from our method. The first baseline (denoted as “basic”) is to remove all Mamba layers and boundary-aware constraint from our network. It means that “basic” equals the vanilla Transformer [29]. Then, we introduce ST-Mamba layers with temporal forward SSM (T^f) into “basic” to construct another baseline network “C1”, and further equip ST-Mamba with temporal backward SSM (T^b) to build a baseline network “C2”. Based on “C2”, spatial SSM (S) is incorporated into the ST-Mamba to construct “C3”. Hence, “C3” is equal to removing the boundary-aware constraint from the training of our network. Table 3 reports the results of our method and four baseline networks. Compared to “basic”, “C1” has a considerable improvement across all metrics, which indicates that the vanilla SSM

helps explore temporal dependency, thereby improving the segmentation performance in videos. Then, the better Dice and Jaccard results of “C2” over “C1” demonstrate that introducing our bidirectional temporal SSMS can benefit the cross-frame coherence. Furthermore, by adapting SSMS to non-causal information, “C3” advances “C2” with a significant margin of 0.46% in Dice and 0.83% in Recall. Finally, our method outperforms “C3” in terms of Dice, Jaccard and Precision, which indicates that the boundary-aware constraint can further help to enhance the VTUS results.

4 Conclusion

In this paper, we present a Mamba-based framework Vivim to address the challenges of medical video object segmentation, especially in modeling long-range temporal dependencies due to the inherent locality of CNNs and the high computational complexity of the self-attention mechanism. The main idea of Vivim is to introduce the structured state space models with spatiotemporal selective scan, ST-Mamba, into the standard hierarchical Transformer architecture. This facilitates the exploration of single-frame spatial coherence and cross-frame coherence in a computationally cheaper way than using the self-attention mechanism. Experimental results on our collected VTUS dataset and polyp colonoscopy videos reveal that Vivim outperforms state-of-the-art segmentation networks.

References

1. Arnab, A., Deghani, M., Heigold, G., Sun, C., Lučić, M., Schmid, C.: Vivit: A video vision transformer. In: Proceedings of the IEEE/CVF international conference on computer vision. pp. 6836–6846 (2021)
2. Bernal, J., Sánchez, F.J., Fernández-Esparrach, G., Gil, D., Rodríguez, C., Vilarino, F.: Wm-dova maps for accurate polyp highlighting in colonoscopy: Validation vs. saliency maps from physicians. *Computerized medical imaging and graphics* **43**, 99–111 (2015)
3. Bernal, J., Sánchez, J., Vilarino, F.: Towards automatic polyp detection with a polyp appearance model. *Pattern Recognition* **45**(9), 3166–3182 (2012)
4. Borse, S., Wang, Y., Zhang, Y., Porikli, F.: Inverseform: A loss function for structured boundary-aware segmentation. In: Proceedings of the IEEE/CVF conference on computer vision and pattern recognition. pp. 5901–5911 (2021)
5. Canny, J.: A computational approach to edge detection. *IEEE Transactions on pattern analysis and machine intelligence* (6), 679–698 (1986)
6. Chen, J., Lu, Y., Yu, Q., Luo, X., Adeli, E., Wang, Y., Lu, L., Yuille, A.L., Zhou, Y.: Transunet: Transformers make strong encoders for medical image segmentation. arXiv preprint arXiv:2102.04306 (2021)
7. Fan, D.P., Cheng, M.M., Liu, Y., Li, T., Borji, A.: Structure-measure: A new way to evaluate foreground maps. In: Proceedings of the IEEE international conference on computer vision. pp. 4548–4557 (2017)
8. Fan, D.P., Ji, G.P., Qin, X., Cheng, M.M.: Cognitive vision inspired object segmentation metric and loss function. *Scientia Sinica Informationis* **6**(6) (2021)

9. Fan, D.P., Ji, G.P., Zhou, T., Chen, G., Fu, H., Shen, J., Shao, L.: Pranel: Parallel reverse attention network for polyp segmentation. In: MICCAI. pp. 263–273. Springer (2020)
10. Gu, A., Dao, T.: Mamba: Linear-time sequence modeling with selective state spaces. arXiv preprint arXiv:2312.00752 (2023)
11. He, K., Gkioxari, G., Dollár, P., Girshick, R.: Mask r-cnn. In: Proceedings of the IEEE international conference on computer vision. pp. 2961–2969 (2017)
12. He, K., Zhang, X., Ren, S., Sun, J.: Deep residual learning for image recognition. In: Proceedings of the IEEE conference on computer vision and pattern recognition. pp. 770–778 (2016)
13. Huang, Q., Huang, Y., Luo, Y., Yuan, F., Li, X.: Segmentation of breast ultrasound image with semantic classification of superpixels. *Medical Image Analysis* **61**, 101657 (2020)
14. Jha, D., Smedsrud, P.H., Riegler, M.A., Halvorsen, P., de Lange, T., Johansen, D., Johansen, H.D.: Kvasir-seg: A segmented polyp dataset. In: MultiMedia Modeling: 26th International Conference, MMM 2020, Daejeon, South Korea, January 5–8, 2020, Proceedings, Part II 26. pp. 451–462. Springer (2020)
15. Jha, D., Smedsrud, P.H., Riegler, M.A., Johansen, D., De Lange, T., Halvorsen, P., Johansen, H.D.: Resunet++: An advanced architecture for medical image segmentation. In: 2019 IEEE international symposium on multimedia (ISM). pp. 225–2255. IEEE (2019)
16. Ji, G.P., Chou, Y.C., Fan, D.P., Chen, G., Fu, H., Jha, D., Shao, L.: Progressively normalized self-attention network for video polyp segmentation. In: MICCAI. pp. 142–152. Springer (2021)
17. Kalman, R.E.: A new approach to linear filtering and prediction problems (1960)
18. Li, J., Zheng, Q., Li, M., Liu, P., Wang, Q., Sun, L., Zhu, L.: Rethinking breast lesion segmentation in ultrasound: A new video dataset and a baseline network. In: MICCAI. pp. 391–400. Springer (2022)
19. Liang, Y., Li, X., Jafari, N., Chen, J.: Video object segmentation with adaptive feature bank and uncertain-region refinement. *Advances in Neural Information Processing Systems* **33**, 3430–3441 (2020)
20. Lin, Z., Lin, J., Zhu, L., Fu, H., Qin, J., Wang, L.: A new dataset and a baseline model for breast lesion detection in ultrasound videos. In: MICCAI. pp. 614–623. Springer (2022)
21. Ma, J., Li, F., Wang, B.: U-mamba: Enhancing long-range dependency for biomedical image segmentation. arXiv preprint arXiv:2401.04722 (2024)
22. Oh, S.W., Lee, J.Y., Xu, N., Kim, S.J.: Video object segmentation using space-time memory networks. In: Proceedings of the IEEE/CVF International Conference on Computer Vision. pp. 9226–9235 (2019)
23. Perazzi, F., Khoreva, A., Benenson, R., Schiele, B., Sorkine-Hornung, A.: Learning video object segmentation from static images. In: Proceedings of the IEEE conference on computer vision and pattern recognition. pp. 2663–2672 (2017)
24. Ronneberger, O., Fischer, P., Brox, T.: U-net: Convolutional networks for biomedical image segmentation. In: International Conference on Medical Image Computing and Computer-Assisted Intervention. pp. 234–241. Springer (2015)
25. Tajbakhsh, N., Gurudu, S.R., Liang, J.: Automated polyp detection in colonoscopy videos using shape and context information. *IEEE transactions on medical imaging* **35**(2), 630–644 (2015)
26. Vaswani, A., Shazeer, N., Parmar, N., Uszkoreit, J., Jones, L., Gomez, A.N., Kaiser, Ł., Polosukhin, I.: Attention is all you need. *Advances in neural information processing systems* **30** (2017)

27. Wang, W., Xie, E., Li, X., Fan, D.P., Song, K., Liang, D., Lu, T., Luo, P., Shao, L.: Pyramid vision transformer: A versatile backbone for dense prediction without convolutions. In: Proceedings of the IEEE/CVF international conference on computer vision. pp. 568–578 (2021)
28. Wang, Y., Deng, Z., Hu, X., Zhu, L., Yang, X., Xu, X., Heng, P.A., Ni, D.: Deep attentional features for prostate segmentation in ultrasound. In: Medical Image Computing and Computer Assisted Intervention–MICCAI 2018: 21st International Conference, Granada, Spain, September 16–20, 2018, Proceedings, Part IV 11. pp. 523–530. Springer (2018)
29. Xie, E., Wang, W., Yu, Z., Anandkumar, A., Alvarez, J.M., Luo, P.: Segformer: Simple and efficient design for semantic segmentation with transformers. *Advances in Neural Information Processing Systems* **34**, 12077–12090 (2021)
30. Yang, Y., Wang, S., Zhu, L., Yu, L.: Hcdg: A hierarchical consistency framework for domain generalization on medical image segmentation. *arXiv preprint arXiv:2109.05742* (2021)
31. Zhang, R., Li, G., Li, Z., Cui, S., Qian, D., Yu, Y.: Adaptive context selection for polyp segmentation. In: MICCAI. pp. 253–262. Springer (2020)
32. Zheng, S., Lu, J., Zhao, H., Zhu, X., Luo, Z., Wang, Y., Fu, Y., Feng, J., Xiang, T., Torr, P.H., et al.: Rethinking semantic segmentation from a sequence-to-sequence perspective with transformers. In: Proceedings of the IEEE/CVF conference on computer vision and pattern recognition. pp. 6881–6890 (2021)
33. Zhou, Z., Rahman Siddiquee, M.M., Tajbakhsh, N., Liang, J.: Unet++: A nested u-net architecture for medical image segmentation. In: Deep learning in medical image analysis and multimodal learning for clinical decision support, pp. 3–11. Springer (2018)
34. Zhu, L., Liao, B., Zhang, Q., Wang, X., Liu, W., Wang, X.: Vision mamba: Efficient visual representation learning with bidirectional state space model. *arXiv preprint arXiv:2401.09417* (2024)